NUMERICAL INVESTIGATION OF FLOW BEHAVIOUR OF AN IMPINGING JET IN A CROSS-FLOW ON A WALL MOUNTED CUBE USING RSM AND $\overline{v^2}$-f TURBULENCE MODELS

D. Rundström
Department of Technology and Build Environment
University of Gävle, S-801 76 Gävle, Sweden
drm@hig.se,

B. Moshfegh
Department of Mechanical Engineering
Linköping University, S-581 83 Linköping, Sweden
bahmo@ikp.liu.se

ABSTRAC

The current trends towards the greater functionality of electronic devices are resulting in a steady increase in the amount of heat dissipated from electronic components. Forced channel flow is frequently used to remove heat from the walls of the channel where a PCB with a few high heat-dissipating components is located. The overall cooling strategy thus must not only match the overall power dissipation load, but also address the requirements of the "*hot*" components. In combating the whole thermal load with forced channel flow, excessive flow rates will be required. The aim of the present study is to investigate if targeted cooling systems in combination will low-velocity channel flow can improve the thermal performance of the systems.

The objective of this study is to investigate the possibility to predict the mean velocity field and the turbulence characteristics with two different RANS turbulence models, i.e. the $\overline{v^2}$-f model and a Reynolds-Stress-Model (RSM) with a two-layer model in the near-wall region. The geometrical case is a channel with a cube in the middle of the base plate and two inlets, one horizontal channel flow and one vertical impinging jet above the cube.

The numerical predictions are validated against a PIV-measurement with identical geometrical and flow set-up. The time average velocity components and the Reynolds stresses are compared at different positions in the domain.

1. INTRODUCTION

Impinging jets are used for many industrial applications where high heat and mass transfer rates are required (e.g. drying of paper and textiles, tempering of glass and cooling of electronic components. The current trends towards the miniaturization of electronic devices, greater functionality and increasing processing speed are resulting in a steady increase in the amount of heat dissipated from the electronic components. Forced channel flow is frequently used for removing heat from the walls of the channel where printed circuit boards (PCBs) are located. In a typical electronic system, the PCB will contain one or very few high heat dissipating components. The overall cooling strategy thus must not only match the overall power dissipation load, but also address the requirements of the "*hot*" components. In combating the whole thermal load with forced channel flow, excessive flow rates will be required. One possible method to face this problem is to divide the channel flow in an impinging jet and a low-velocity channel flow. Where the low-velocity channel flow can manage the cooling requirement of the low generating components and the impinging jet can be forced directly on the "*hot*" components and provide a good thermal performance.

Extensive experimental and numerical research has been carried out to predict the flow and heat transfer characteristics in the stagnation region of an impinging jet. Most investigations have been focused on axisymmetric round jets impinging normally on a flat surface. The earlier investigations by Behnia *et al.* (1998) have shown that the most common two-equation RANS models e.g. the standard k-ε model, over-predict the heat transfer rate in the stagnation region by over 100 percent. This case has also been simulated with the $\overline{v^2}$-f model, e.g. by Behnia *et al.* (1998), with satisfactory agreement with the experimental data. Launder *et al.* (1992) used a low-Re model with the Yap correlation added to the ε-equation and three different Reynolds stress models to simulate the mean velocity field, Reynolds stresses and the heat transfer rate.

Two natural choices of RANS-turbulence models are the $\overline{v^2}$-f model developed by Durbin (1991 and 1996) and a suitable Reynolds stress model (RSM) with a two-layer model in the near-wall region. One advantage with the $\overline{v^2}$-f model is that fact that the model is valid the whole way from the other region through the sub-layer region i.e. no wall, or damping functions are used in the near-wall treatment. The model has shown satisfactory results for a range of flows types in the near-wall region. A range of different Reynolds stress models (RSM) has been developed under the last decades; see Launder *et al.* (1975, 1977, 1989 and 1992). It is well established that the RSM:s show better accuracy than the most common two-equation eddy-viscosity models for flows types where curvature effects and stagnation regions have an important influence.

The purpose with this study is to provide a thorough understanding of the physics in this complex flow and investigate the possibility to predict the mean velocity field and the turbulence characteristics with two different steady state RANS turbulence models.

2. COMPUTATIONAL SET-UP AND NUMERICAL SCHEME

2.1 Geometrical set-up and boundary conditions

The computational domain is a rectangular channel with a cube in the middle of the bottom wall (see Figure 2.1). The channel has two inlets, one horizontal channel flow with a "low" velocity and one vertical impinging jet with a "high" velocity. The impinging jet enters through a circular nozzle in the middle of the top plate. The geometrical details and fluid properties are summarised in Table 2.1. *Sx*, *Sz* are the stream-wise and span-wise dimensions respectively.

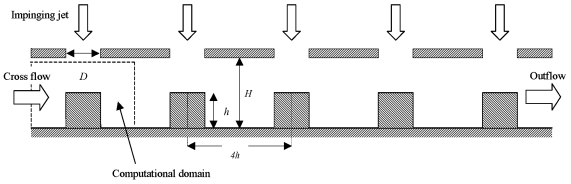

Figure 2.1. Computational set-up.

The following boundary conditions are used: The top and bottom walls have no-slip conditions, symmetric boundary conditions are used for the sidewalls and zero gradient condition for the outflow. The mean velocities of cross-flow and the impinging jet are 1.66 and 4.79 m/s. The velocity profile and the turbulent properties at the inlet of the cross-flow are given from a separate fully developed channel flow simulation with respective turbulence model. A curve fit from the PIV-measurement is used for the velocity profile of the impinging jet and average value of the turbulence intensity also derived from the measurement.

Table 2.1. Geometrical and flow details.

D	12 mm	Re_j	3936
h	15 mm	Re_c	3410
H	$2h$	ρ	1.225 kg/m^3
Sx, Sz	$4h$	μ	$1.789 \cdot 10^{-5}$ kg/ms

2.2 Governing equations

The steady state three-dimensional incompressible continuity and Navier-Stokes equations are given by

$$\frac{\partial U_i}{\partial x_i} = 0 \tag{2.1}$$

$$\frac{\partial (U_j U_i)}{\partial x_j} = -\frac{1}{\rho}\frac{\partial p}{\partial x_i} + \frac{\partial}{\partial x_j}\left(\nu \frac{\partial U_i}{\partial x_j} - \overline{u_i' u_j'}\right) \tag{2.2}$$

2.3 The $\overline{v^2}$-f model

The $\overline{v^2}$-f model used the eddy viscosity hypothesis for the unknown Reynolds stresses given by

$$-\overline{u_i' u_j'} = \nu_t S_{ij} - \frac{2}{3}\delta_{ij} k \tag{2.3}$$

where S_{ij} is the strain rate, k is the turbulent kinetic energy and ν_t is the turbulent viscosity given by

$$\nu_t = C_\mu \overline{v^2} T \tag{2.4}$$

where $\overline{v^2}$ is the wall normal stress. T is the turbulent time-scale given by

$$T = \min\left[\max\left(\frac{k}{\varepsilon}, C_T\left(\frac{\nu}{\varepsilon}\right)^{1/2}\right), \frac{\alpha}{\sqrt{3}}\frac{k}{\overline{v^2} C_\mu \sqrt{2 S_{ij} S_{ij}}}\right] \tag{2.5}$$

The transport equation for $\overline{v^2}$ is given by

$$\frac{\partial}{\partial x_j}\left(U_j \overline{v^2}\right) = \frac{\partial}{\partial x_j}\left[\left(\nu + \frac{\nu_t}{\sigma_k}\right)\frac{\partial \overline{v^2}}{\partial x_j}\right] + kf - \frac{\overline{v^2}}{k}\varepsilon \tag{2.6}$$

where ε is the dissipation rate of k and where f is the elliptic relaxation factor given by

$$f - L^2 \frac{\partial^2 f}{\partial x_i \partial x_i} = \frac{(C_1 - 1)}{T}\left(\frac{2}{3} - \frac{\overline{v^2}}{k}\right) + C_2 2 \frac{\nu_t}{k} S_{ij} S_{ij} \tag{2.7}$$

where L is the turbulent length scale given by

$$L = C_L \max\left[\min\left(\frac{k^{3/2}}{\varepsilon}, \frac{1}{\sqrt{3}}\frac{k^{3/2}}{\overline{v^2} C_\mu \sqrt{2 S_{ij} S_{ij}}}\right), C_\eta\left(\frac{\nu^3}{\varepsilon}\right)^{1/4}\right] \tag{2.8}$$

The transport equations for turbulent kinetic energy, k, and dissipation rate, ε, are given by

$$\frac{\partial}{\partial x_j}\left(U_j k\right) = \frac{\partial}{\partial x_j}\left[\left(\nu + \frac{\nu_t}{\sigma_k}\right)\frac{\partial k}{\partial x_j}\right] + 2\nu_t S_{ij} S_{ij} - \varepsilon \tag{2.9}$$

$$\frac{\partial}{\partial x_j}\left(U_j \varepsilon\right) = \frac{\partial}{\partial x_j}\left[\left(\nu + \frac{\nu_t}{\sigma_\varepsilon}\right)\frac{\partial \varepsilon}{\partial x_j}\right] + C_{\varepsilon 1}^{*} 2\nu_t \frac{S_{ij} S_{ij}}{T} - C_{\varepsilon 2}\frac{\varepsilon}{T} \tag{2.10}$$

The following constants have been used in the $\overline{v^2}$-f model: C_μ = 0.22, C_T = 6, σ_k = 1, C_1 = 1.4, C_2 = 0.3, C_L = 0.23, C_η = 70, α = 0.6, σ_ε = 1.3, $C_{\varepsilon 1}$ = 1.4, $C_{\varepsilon 2}$ = 1.9 and $C_{\varepsilon 1}^{*} = C_{\varepsilon 1}\left(1 + 0.045\sqrt{k/\overline{v^2}}\right)$

2.4 Reynolds Stress Model (RSM)

The transport equations of Reynolds stresses can be written as

$$\underbrace{\frac{\partial}{\partial x_k}\left(U_k \overline{u_i' u_j'}\right)}_{C_{ij}} = \underbrace{\frac{\partial}{\partial x_k}\left[-\overline{u_i' u_j' u_k'} - \frac{\overline{p'}}{\rho}\left(\delta_{jk} u_i' + \delta_{ik} u_j'\right) + \nu \frac{\overline{\partial u_i' u_j'}}{\partial x_k}\right]}_{D_{ij}}$$

$$\underbrace{-\overline{u_i' u_k'}\frac{\partial U_j}{\partial x_k} - \overline{u_j' u_k'}\frac{\partial U_i}{\partial x_k}}_{P_{ij}} \underbrace{- 2\nu \overline{\frac{\partial u_i'}{\partial x_k}\frac{\partial u_j'}{\partial x_k}}}_{\varepsilon_{ij}} + \underbrace{\overline{\frac{p'}{\rho}\left(\frac{\partial u_i'}{\partial x_j} + \frac{\partial u_j'}{\partial x_i}\right)}}_{\Phi_{ij}} \tag{2.11}$$

D_{ij} is the modelled diffusion part given by

$$D_{ij} = \frac{\partial}{\partial x_k}\left(\nu \frac{\partial \overline{u_i' u_j'}}{\partial x_k}\right) + \frac{\partial}{\partial x_k}\left(\frac{\nu_t}{\sigma_k}\frac{\partial \overline{u_i' u_j'}}{\partial x_k}\right) \tag{2.12}$$

The first term on the right hand side of Eq. (2.12) is the molecular transport and the second term is the modelled version of turbulent transport proposed by Lien and Leschziner (1994). The turbulent viscosity, ν_t, is modelled as

$$\nu_t = C_\mu \frac{k^2}{\varepsilon} \tag{2.13}$$

where k and ε are turbulent kinetic energy and dissipation rate of, k. The transport equation of turbulent dissipation rate is given by

$$\frac{\partial}{\partial x_j}\left(U_j \varepsilon\right) = \frac{\partial}{\partial x_j}\left[\left(\nu + \frac{\nu_t}{\sigma_\varepsilon}\right)\frac{\partial \varepsilon}{\partial x_j}\right] - C_{\varepsilon 1}\overline{u_i' u_j'}\frac{\partial U_i}{\partial x_j}\frac{\varepsilon}{k} - C_{\varepsilon 2}\frac{\varepsilon^2}{k} \tag{2.14}$$

The dissipation part, ε_{ij}, is modelled with the isotropic dissipation assumption as

$$\varepsilon_{ij} = \frac{2}{3}\delta_{ij}\varepsilon \tag{2.15}$$

The pressure-strain term, Φ_{ij}, is modelled by a linear approach proposed by Launder *et al.* (1975, 1977). The RSM used a near wall treatment for the pressure-strain term proposed by Launder and Shima (1989). The transport equation of turbulent kinetic energy is used to obtain the boundary condition given by

$$\frac{\partial}{\partial x_j}\left(U_j k\right) = \frac{\partial}{\partial x_j}\left[\left(\nu + \frac{\nu_t}{\sigma_k}\right)\frac{\partial k}{\partial x_j}\right] - \overline{u_i' u_j'}\frac{\partial U_i}{\partial x_j} - \varepsilon \tag{2.16}$$

The following constants have been used in the RSM model: $C_\mu = 0.09$, $\sigma_k = 0.82$, $\sigma_\varepsilon = 1.0$, $C_{\varepsilon 1} = 1.44$ and $C_{\varepsilon 2} = 1.92$, $C_1 = 1.8$, $C_2 = 1.6$, $C_1^w = 0.5$, $C_2^w = 0.3$, $\kappa = 0.4187$. Details about the modelling of the linear pressure strain term and the two-layer model for a near-wall region can be find in the Fluent Manuals (2003).

2.3 Numerical details

The finite volume code Fluent 6.1.18 is used to numerically simulate the air flow pattern of the impinging jet in a cross-flow condition. The governing equations are solved with a segregated scheme and the SIMPLE algorithm solves the pressure-velocity coupling see Table 2.2 for more information about the numerical details.

Table 2.2. Numerical scheme

Grid	Staggered grid
Pressure-Velocity-Coupling algorithm	SIMPLE
Discretization schema:	
Non-linear terms	Second – order upwind schema
Viscous terms	Second – order central scheme

The mesh consists of 881 832 structured hexahedral cells. There are 42 × 42 cells near the sidewalls of the cube. The top of the cube consists of a total of 5876 cells. The circular inlet and the region under the impinging jet consist of 2516 cells in the *xz*-plane. The mesh is refined enough near the solid walls ($y^+ \approx 1$) to solve the all boundary layer with the two-layer model.

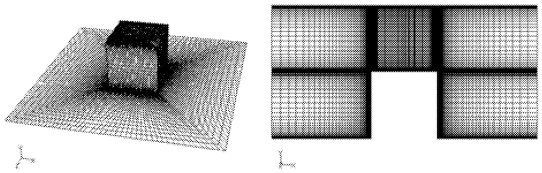

Figure 2.2. Computational grid, perspective view (left figure), side view (right figure).

3. EXPERIMENTAL DETAILS

3.1 Experimental set-up

The experimental set-up is shown in Figure 2.1. The experimental equipment consists of a wind tunnel with five in-line mounted cubes in the middle of the tunnel. The size of the cubes h is 15 mm and the distances between the cubes S_x are 60 mm. The tunnel has a height H of 30 mm and a width of 360 mm. One impinging jet is positioned above each cube. The impinging jets are forced through circular holes with a diameter D of 12 m. The centre of the impinging jets and the cubes are identical. The impinging jets are provided by air from a separate channel placed above the top plate. All measurements are carried out at the first cube (see Figure 2.1).

3.2 PIV-Measurement

The time-average velocity field and the Reynolds components have been measured in the *xy*-plane with a PIV-system. The PIV-equipment included a double pulsed Nd:YAG laser with a pulse energy of 25 mJ. The laser was used to produce an approximately 1 mm thick light sheed that illuminated the seed particles in the flow. A PCO Sensicam camera recorded images of the seed particles in the light sheet. For each plane 1000 images pairs where acquired and the commercial software VidPIV Rowan v4.0 was used to analyse the images.

These measurements have been carried out at the Department of Applied Physics, Delft University of Technology, Delft, The Netherlands, see Tummers *et al* (2005).

4. COMPUTATIONAL RESULTS

4.1 Flow configuration

The flow field shows a complex behaviour (see Figure 4.1) and there are several flow related phenomena that can affect the cooling performance. For example the position of the stagnation point on top of the cube is an important factor for the prediction of heat transfer rate on top of the cube and the separations from the top of the cube plays an important effect on the heat transfer mechanisms at the other four walls.

The cross-flow has several flow related effects on the impinging jet and the separations from the top of the cube. Figure 4.2 shows the characteristic horseshoe shape when the streamlines from the cross-flow collide with the separated flow from the top of the front face, which results in a re-circulating vortex flow around the cube. A similar horseshoe

vortex is arising around the impinging jet (see Figure 4.2), which results in a deformation of the cross section of the impinging jet and produces two re-circulating wake vortices and the counter-rotating vortex pairs (CVP). The impinging jet creates a down-wash flow with a spiral shaped feature due the vortex pair (see Figure 4.2).

The region behind the rear face of the cube consists of two vertical re-circulating vortices (perpendicular to the *xz*-plane) and one powerful horizontal vortex (perpendicular to the *xy*-plane) near the top of the cube (see Figures 4.1 and 4.2). These three vortices occur due to the separations from the sharp edges of the rear face. The vortices results in a spiral shaped up-wash flow near the rear face.

The separation from the front face results in two small vertical vortices near each sidewall and the separated flow from the top creates an up-wash flow near the sidewalls (see Figure 4.2). The up-wash flow is most significant near the reattachment points at the rear part of the sidewalls (see Figure 4.2) where the *x*-momentum is low and the separations from the top are most powerful.

The cross-flow in the lower part of the channel curls around the front face of the cube. The position of the stagnation point at the front face is approximately located at $y = 0.84h$. The downwash flow from the front face results in a re-circulating vortex near the base of the front face (see Figure 4.2).

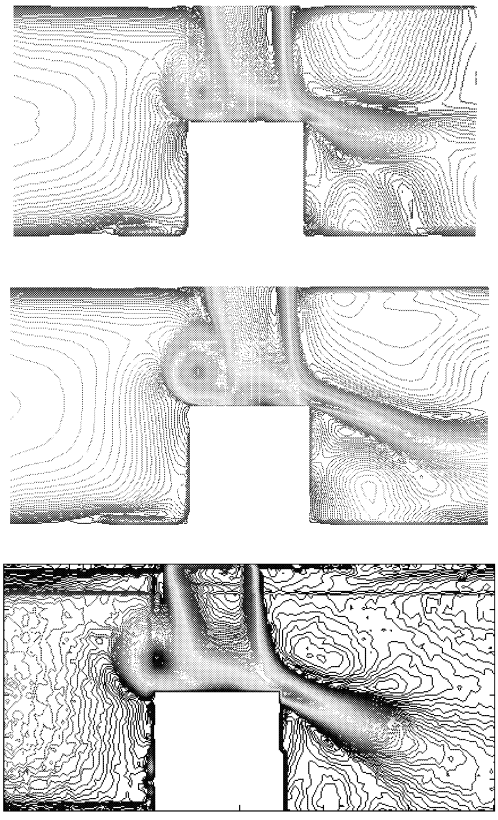

Figure 4.1. Contours of velocity magnitude in the *xy*-plane, $z/h = 2$, RSM (upper), $\overline{v^2}$-f model (middle), PIV-measurement (lower).

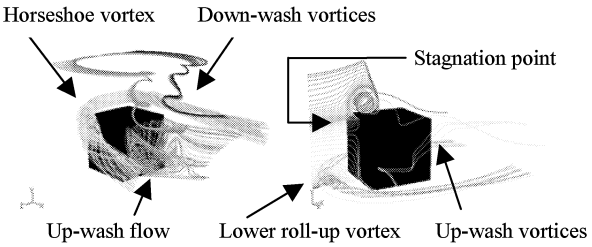

Figure 4.2. Path lines from the simulation with the RSM.

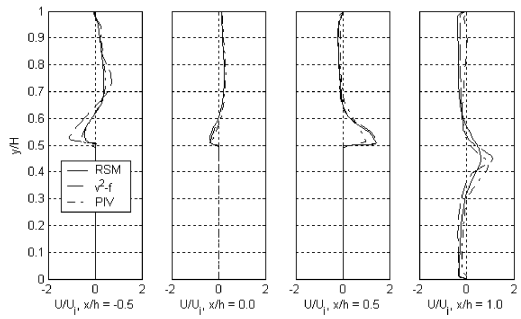

Figure 4.3. x-velocity component (U/U_j) above the top of the cube.

Figure 4.3 shows the normalized x-velocity component (U/U_j) as a function of the vertical distance (y/H) in the region above the top and behind the rear side of the cube. Each diagram represents different positions in x-direction at the centre of the cube. The first diagram represents the line parallel with the front face of the cube (i.e. $x/h = -0.5$) and the four following diagrams represent the following x-positions $x/h = -0.25$, $x/h = 0.0$, $x/h = 0.25$, $x/h = 0.5$ and $x/h = 1.0$.

Both models show good agreement with the PIV-measurement near the stagnation region (see diagrams no. 2 and 3 from the left in Figure 4.3). The $\overline{v^2}$-f model seems to over-predict the magnitude of the velocity in the re-circulating region on top of the cube and the RSM shows good agreement with the PIV-measurement in this region (see diagram no. 1 and 2 from the left in Figure 4.3). The $\overline{v^2}$-f model seems also to over-predict the size of the re-circulating vortex (see diagram no. 1 from the left in Figure 4.3). Both models seem to over-predict the velocity magnitude of the powerful separations at the rear part of the top face (see diagram no. 1 from the right in Figure 4.3).

The maximal velocity behind the rear face occurs at higher positions in both simulations than in the PIV-measurement (see diagram no. 4 from left in Figure 4.3). It can also be noted that the $\overline{v^2}$-f model shows less diffusivity than the RSM and the PIV-measurement, which results in a higher maximum value of the velocity. The $\overline{v^2}$-f model also shows the largest back-flow in the lower region.

4.2 Reynolds Stress

Figure 4.4 shows the normalized $\overline{u'^2}$-Reynolds stress as a function of the vertical distance (y/H) in the region above the top and behind the rear side of the cube. The representation of each diagram is identical with Figure 4.3.

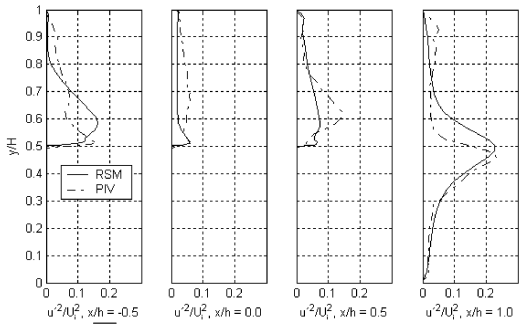

Figure 4.4. $\overline{u'^2}$-Reynolds stress above the top of the cube.

The predicted $\overline{u'^2}$-Reynolds stresses are in good agreement with the PIV-measurement in the stagnation region (x/h = 0.0). The maximum value near the top of the cube is located at approximately the same coordinates and the magnitudes of the peak are also in good agreement (see Figure 4.4). The region above the rear edge shows a significant second peak above the first one (see diagram no. 2 from the left in Figure 4.4.). The RSM and the PIV-measurement show a pronounced peak in the near wall region in the first diagram in Figure 4.4 and a second peak is observed above the first one in both RSM and in PIV-measurement. The upper peak is much greater in the RSM and the maximum is located in a lower region than in the PIV-measurement. A third peak can also be observed in the PIV-measurement (see diagram no. 1 in Figure 4.4) but not in the RSM. These peaks can be explained by the re-circulating vortex at the front of the cube. Diagram no. 4 in Figure 4.4 shows that the maximum value and the positions of the peaks are approximately identical after the rear side of the cube. Another observation from Figure 4.4 is that the RSM is more diffusive than the PIV-measurement in the region above the maximum value. The RSM predicts the vertical positions of the maximum in higher regions than the PIV-measurement when $0.5 \leq x/h \leq 1.0$ (see Figure 4.4).

Figure 4.5 shows the normalized $\overline{v'^2}$-Reynolds stress as a function of the vertical distance (y/H) in the region above the top and behind the rear side of the cube. The representation of each diagram is identical with Figure 4.4.

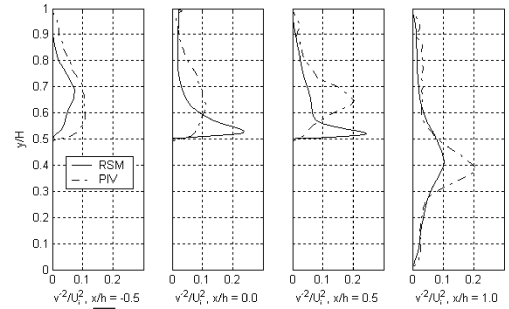

Figure 4.5. $\overline{v'^2}$-Reynolds stress above the top of the cube.

Figure 4.5 shows that a significant peak is observed in the stagnation region ($0.0 \leq x/h \leq 0.5$) in the predicted $\overline{v'^2}$-Reynolds stress at a distance located at approximately y/H = 0.52-0.54. These peaks are not observed in the PIV-measurement (see Figure 4.5). The measured $\overline{v'^2}$-Reynolds stress shows similarities with the measured $\overline{u'^2}$-Reynolds stress in the region above the rear side (see Figure 4.4 and 4.5) where a large maximum occurs at $y/H \approx 0.65$ and a constant decreasing behaviour is observed from the maximum of the peak down to the top of the cube. This maximum is not observed in the RSM and the modelled $\overline{v'^2}$-Reynolds stress shows a similar maximum near the top of the cube as in the middle of the cube. The maximum value of the peak at x/h = 1.0 are higher in the PIV-measurement than in the RSM (see Figure 4.5) which indicates that the net production of $\overline{v'^2}$-Reynolds stress are higher in the PIV-measurement than in the RSM. The maximum is located in a lower region in the PIV-measurement than in the RSM.

Figure 4.6 shows the normalized $\overline{u'v'}$-Reynolds stress as a function of the vertical distance (y/H) in the region above the top and behind the rear side of the cube. The representation of each diagram is identical with Figure 4.5.

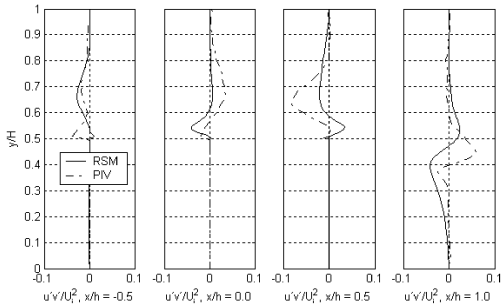

Figure 4.6. $\overline{u'v'}$-Reynolds stress above the top of the cube.

The RSM seems to predict the main characteristics of the $\overline{u'v'}$-Reynolds from the PIV-measurement. The values of the upper peaks in diagram no. 2 and 3 from the left in Figure 4.6 agree well in position but some deviation is observed in the maximum values. Diagram no. 4 from left in Figure 4.6 shows two peaks in the $\overline{u'v'}$-Reynolds stress in the free shear region from the separations behind the rear side of the cube. The peaks are located at higher positions in the RSM than in the PIV-measurement, which indicates that the measured separations from the top of the cube force more against the bottom plate than in the RSM. It can also be observed that the upper (positive) peak is larger in the PIV-measurement than the RSM. The opposite trend is observed for the lower (negative) peak where the RSM shows the highest maximum value (see Figure 4.6).

Figure 4.7 shows the normalized kinetic energy k as a function of the vertical distance (y/H) in the region above and behind the rear side of the cube. The representation of each diagram is identical with Figure 4.6.

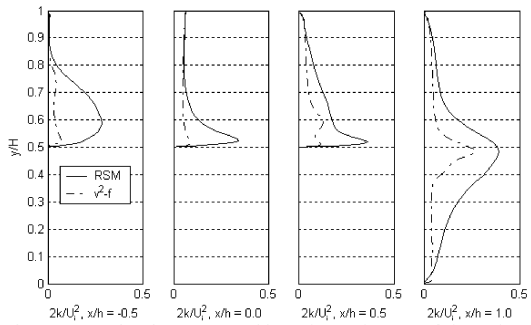

Figure 4.7. Kinetic energy, $2k/U_j$, above the top of the cube.

Figure 4.7 shows that the level of kinetic energy is significant higher in the RSM than in the $\overline{v^2}$-f model particular in the stagnation region. A peak is observed near the top of the cube in both models and the RSM predicts the highest maximum of the peak in all positions above the cube (see Figure 4.7). Diagram no. 3 from left in Figure 4.7 shows that the RSM produces a higher level of turbulent kinetic energy in the shear regions between the impinging jet and the cross-flow. Another significant difference between the models is observed in the region above the front side where the maximum of the peak from the RSM is located at a higher position than in the $\overline{v^2}$-f model. The higher production of k in the stagnation region results in a higher level of kinetic energy at the separations from the rear part of the top in the RSM than in the $\overline{v^2}$-f model (see diagram no. 3 and 4 from left in Figure 4.7). The location of the maximum is approximately identical for both models.

5. CONCLUSIONS AND DISCUSSION

The investigation has shown that two models can predict the mean velocity and the turbulence characteristics for an impinging jet in the cross-flow with satisfactory results. The flow structure is highly complex and the turbulence models have to predict several flow-related phenomena such as stagnation points, separations, re-circulating and curvature effects. Both models predict the mean velocity field well in the stagnation region but the $\overline{v^2}$-f model seems to have more problem than the RSM to predict the turbulent diffusion in the free shear region (i.e. far from the walls). The RSM seems to predict the Reynolds stresses well in all regions except for the stagnation region above the cube where the $\overline{v^2}$-Reynolds stress seems to be over-predicted. The main difference between the models is that the RSM produces a higher level of turbulent kinetic energy (k) than the $\overline{v^2}$-f model in all regions and the largest differences are in the stagnation region at the top of the cube. This lower turbulence intensity in the $\overline{v^2}$-f model seems to results in lower diffusivity in the free shear regions, which obviously can be observed in the separated flow from the top of the cube.

These are the first verification results from an ongoing research project and further investigations are planned both numerically and experimentally. The next verification study will be focused on the heat transfer rate near the cube. Another interesting aspect to study is the unsteady interaction between the impinging jet and the cross-flow and how this interaction will affect the thermal performance. Unsteady RANS and Large-Eddy Simulation (LES), will be used to capture the unsteady predictions of the flow structure. The authors also intend to make an extensive parameter study and investigate the influence of the nozzle-to-plate distance, nozzle geometry, nozzle position and nozzle angle on the airflow pattern around the cube and the surface temperature of the cube.

Acknowledgments

The authors gratefully acknowledge the funding received from the KK Foundations, Ericsson AB, Nokia AB and University of Gävle. The authors wish to express their gratitude to Dr. Mark Tummers and Professor Hanjalic at Delft University of Technology for their experimental support throughout this study.

References

Behnia, M., Parniex, S., Durbin, P., Numerical study of turbulent heat transfer in confined and unconfined impinging jets, *International Journal of Heat and Fluid Flow,* vol. 20, pp. 1-9, 1998.

Chen H. C., Patel, V. C., Near-wall turbulence models for complex flows including separation, *AIAA-Journal*, vol. 26, pp. 641-648, 1988.

Copper, D., Jackson, D. C., Launder, B. E., Liao, G. X., Impinging jet studies for turbulence models assessment-I. Flow-field experiments, *International Journal of Heat and Mass Transfer,* vol. 36, pp. 2675-2684, 1992.

Craft, T. J., Graham, L. J. W., Launder, B. E., Impinging jet studies for turbulence models assessment-II. An examination of the performance of four turbulence models, *International Journal of Heat and Mass Transfer,* vol. 36, pp. 2685-2697, 1992.

Durbin, P. A., Application of a near-wall turbulence model to boundary layers and heat transfer, *International Journal of Heat and Fluid Flow,* vol. 14, pp. 316-322, 1993.

Durbin, P., Near-wall turbulence closure modelling without damping function, *Theoretical and Computational Fluid Dynamics*, vol. 3, pp. 1-13, 1991.

Durbin, P. A., On the k-ε stagnation point anomaly, *International Journal of Heat and Fluid Flow,* vol. 17, pp. 89-90, 1996.

Durbin, P., Separated flow computations with the k-ε-v^2 model, *AIAA-Journal*, vol. 33, pp. 659-664, 1995.

Gibson, M. M., Launder, B. E., Ground effects on pressure fluctuations in the atmospheric boundary layer, *Journal of Fluid Mechanics*, vol. 86, pp. 491-511, 1977.

Fluent 6.1, Fluent Manuals, Fluent Inc. January 2003.

Launder, B. E., Second-moment closure: present... and future?, *International Journal of Heat and Fluid Flow*, vol. 10, pp. 282-300, 1989.

Launder, B. E., Reece, G. J., Rodi, W., Progress in the development of a Reynolds-stress turbulence closure, *Journal of Fluid Mechanics*, vol. 68, pp. 537-566, 1975.

Launder, B. E., Shima, N., Second-moment closure for near-wall sublayer: Development and application, *AIAA-Journal*, vol. 27, pp. 1319-1325, 1989.

Lee, J. and Lee, S.J., Stagnation region heat transfer of a turbulent axisymmetric jet impingement, *Experimental Heat Transfer*, vol. 12, pp. 137-156, 1999.

Lien, F. S., Leschziner, M. A., Assessment of turbulence transport models including non-linear RNG eddy-viscosity formulation and second moment closure for flow over a backward-facing step, *Computers and Fluids*, vol. 23, pp. 983-1004, 1994.

D. Rundström and B. Moshfegh. Investigation of Flow and Heat Transfer of an Impinging Jet in a Cross-Flow for Cooling of a Heated Cube. Accepted for publication in *ASME-Journal of Electronic Packaging*, 2005.

M.J. Tummers, M.A. Flikweert, K. Hanjalić, R. Rodink and B. Moshfegh, Impinging Jet Cooling of Wall Mounted Cubes. Accepted for presentation at *ERCOFTAC International Symposium on Engineering Turbulence Modelling and Measurements - ETMM6*, Sardinia, Italy, 23-25 May 2005.